

A coupled mathematical model and experimental validation of oxygen transport behavior in the electro-slag refining process

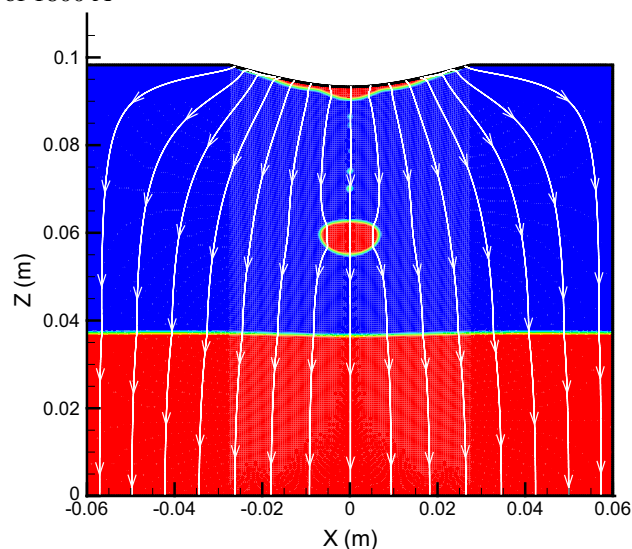
Qiang Wang^{1,2} · Guangqiang Li^{1,2} · Yunming Gao^{1,2} · Zhu He^{1,2} · Baokuan Li³

Received: 22 October 2016 / Accepted: 28 January 2017 / Published online: 17 February 2017
© Springer Science+Business Media Dordrecht 2017

Abstract Electro-slag refining process is widely employed in steel industry for the production of special alloys used in ocean, aeronautics, and nuclear industries. Because of the adverse effect on the ductility of metal, it is critical to remove oxygen in the process. This study established a transient three-dimensional (3D) coupled mathematical model for understanding oxygen transport behavior in the electro-slag refining process. The finite volume method was invoked to simultaneously solve mass, momentum, energy, and species conservation equations. Using the magnetic potential vector, Maxwell's equations were solved, during which the obtained Joule heating and Lorentz force were coupled with the energy and momentum equations, respectively. The movement of metal–slag interface was described through the application of the volume of fluid (VOF) technique. Additionally, an auxiliary metallurgical kinetic module was introduced to determine the electrochemical reaction rate. An experiment was then conducted to validate the model, where the predicted oxygen contents agreed with the measured data within an acceptable accuracy range. Oxygen redistribution in both fluids is clarified: its transport rate at the metal droplet–slag interface is approximately one order of magnitude larger than that at the metal pool–slag interface. Further, the oxygen

content in the metal pool is shown to increase with time, while the content in the slag layer is decreased. In order to effectively remove the oxygen in the metal, one more positive electrode, which is more likely to react with the oxygen, is proposed to be added in the unit.

Graphical abstract Distributions of the electric streamlines and the phase distribution at 151.25 s with a current of 1800 A



✉ Guangqiang Li
liguangqiang@wust.edu.cn

¹ The State Key Laboratory of Refractories and Metallurgy, Wuhan University of Science and Technology, Wuhan, Hubei 430081, China

² Key Laboratory for Ferrous Metallurgy and Resources Utilization of Ministry of Education, Wuhan University of Science and Technology, Wuhan, Hubei 430081, China

³ School of Metallurgy, Northeastern University, Shenyang, Liaoning 110819, China

Keywords Electro-slag refining process · Oxygen transfer · Electrochemical reaction · Numerical simulation

List of symbols

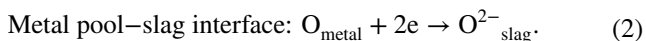
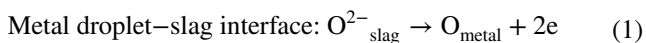
\vec{A} Magnetic potential vector/ $V \text{ s m}^{-1}$
 \vec{B} Magnetic flux density/T
 c Mass percent of oxygen
 c_0 Coefficient in Eqs. (10) and (12)

D	Diffusion coefficient of oxygen/ $\text{m}^2 \text{ s}$
E	Internal energy of mixture phase/ J m^3
F	Faraday law constant/ C mol
\vec{F}_e	Lorentz force/ N m^3
\vec{F}_s	Solute buoyancy force/ N m^3
\vec{F}_t	Thermal buoyancy force/ N m^3
I	Current/ A
\vec{J}	Current density/ A m^2
k	Mass transfer rate/ $\text{kg m}^3 \text{ s}$
k_T	Effective thermal conductivity/ $\text{W m}^{-1} \text{ K}^{-1}$
L	Latent heat of fusion/ J kg
\dot{m}	Melt rate/ kg s
n	Number of electrons entering in the reaction
\vec{n}	Unit normal vector
p	Pressure/ Pa
Q_J	Joule heating/ W m^3
R	Gas constant/ $\text{J mol}^{-1} \text{ K}^{-1}$
S	Source term in Eq. (8)
T	Temperature/ K
t	Time/ s
\vec{v}	Velocity/ m s^{-1}
x, y, z	Cartesian coordinates

1 Introduction

The metallurgical industry has widely employed electro-slag refining technologies to increase the production of special steels for applications in ocean, aeronautics, and nuclear industries [1]. Figure 1 displays a schematic of the electro-slag refining process. During this process, a constant direct current is passed from the metallic positive electrode to the negative baseplate, creating Joule heating in the highly resistive calcium fluoride-based molten slag, the large amount of which is enough to melt the positive electrode. A film of the molten metal is then created at the anode tip, while a droplet is gradually formed within the continuous melting process. The dense metal droplet sinks through the less dense slag, forming a liquid metal pool in a water-cooled mold. During the refining process, the consumable electrode keeps moving downwards, therefore maintaining the circuit's running [2].

Due to oxygen's adverse effect on the ductility of metal products, its removal is one of the most important tasks in the electro-slag refining process. Electrochemical oxygen reactions in the reactor take the following two forms:



At the metal droplet-slag interface, the electrons flow from slag to metal. Therefore, the oxygen ions enter into

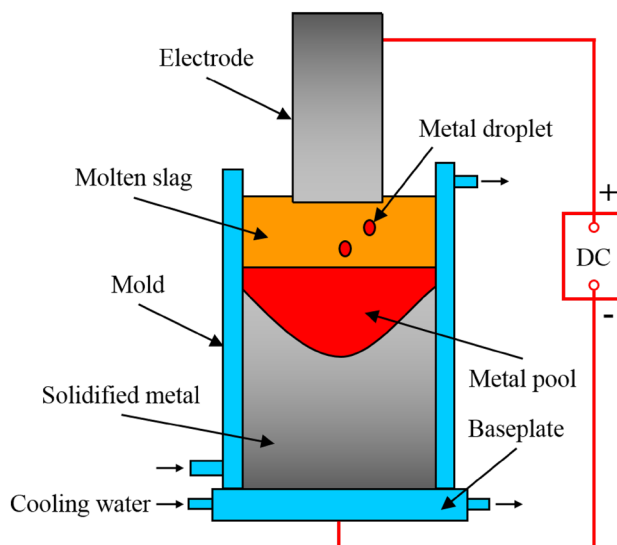


Fig. 1 Schematic of electro-slag refining process used in steel industry

the metal droplet as oxygen atoms, after losing two electrons, and result in oxygen pick-up in the droplet. However, the electrons migrate from metal pool to slag at the metal pool-slag interface, where oxygen atoms in the metal pool capture two electrons and shift into the slag in the ionic state. The oxygen content in the metal pool is therefore reduced. Consequently, final oxygen concentrations in the metal are determined by these two reactions [3, 4]. Moreover, the movement of oxygen ions or atoms during melting has been found to be the rate-limiting step when compared with reaction rate. Oxygen transport during the refining process is supposed to be dramatically affected by coupled physical fields, including the electromagnetic field, flow pattern, and thermal behavior [5].

Several previous experiments were conducted to illustrate oxygen redistribution in the metal and in the slag [6–9]. The obtained results confirm that the mass transfer coefficient immensely depends on current density at the two slag-metal interfaces, as well as the two fluids' motion. Unfortunately, the information obtained from these experiments was limited due to the opaque reactor and the harsh environment. Moreover, the electric current, velocity, and temperature fields were unknown. However, given the difficulty of performing experiments on a real device, along with the continuous increase of computation resources, numerical simulation is an adequate way to provide useful insights into oxygen transport in this process. Prior efforts have been made to numerically investigate electromagnetism, two-phase flow, and temperature distribution during the electro-slag refining process [10–13]. The current induces a magnetic field, while the interaction between the magnetic field and the current gives rise to an inward

Lorentz force. The slag and metal are driven to flow under the combined effect of Lorentz and buoyancy forces. In a prior study, Josson et al. proposed a new coupled computational fluid dynamic (CFD) and kinetic module to describe the sulfur transfer between the slag and the metal in a gas-stirred ladle [14]. A metallurgical kinetic module was used to represent the desulfurization mechanism. The CFD module solved relevant thermodynamic parameters affected by the flow and temperature fields, including sulfide capacity and oxygen activity. In another study, Danilov used a 3D mathematical model to demonstrate ion migration due to electrochemical reaction and particle dissolution [15]. A homogeneous mixture model and species conservation equation defined the redistribution of the ion concentration in the reactor. Moreover, a charge balance equation described the current density profile. Sen et al. established a two-dimensional mathematical model for electrochemical magnetohydrodynamics [16]. In order to observe the kinetics of the heterogeneous electrode reactions, the Butler–Volmer module was used to obtain the faradaic current density. They also studied the interplay of Lorentz force, convection, and redox species concentration distribution.

As discussed above, the oxygen transport induced by the electrochemical reaction in the electro-slag refining process remains unclear. Few attempts have been made to numerically investigate oxygen transport coupled with electromagnetic, velocity, and temperature fields. For these reasons, the authors were motivated to create a transient 3D comprehensive model that would understand oxygen transport between the metal and the slag. A metallurgical kinetic module was used to solve the electrochemical reaction, while the physical fields were simultaneously taken into consideration. Finally, an experiment was conducted to properly validate the model.

2 Mathematical model

2.1 Assumptions

In order to maintain a reasonable computational time, this study’s model relied on the following assumptions:

1. The domain included the slag and the metal, while atmosphere was disregarded [17].
2. The two fluids were incompressible Newtonian fluids. The slag and metal densities were a function of temperature, and the slag’s electrical conductivity depended on the temperature. Other metal and slag properties were assumed to be constant [2].
3. Solidification behavior was not taken into account [18].
4. The slag and the metal were assumed to be electrically insulated from the mold [12].

5. The electrons participating in the reaction were assumed to be provided by the current. Thermochemical reactions between the oxygen and active elements, such as aluminum, manganese, and silicon in the metal, were not included.
6. Oxygen in the slag was all provided by the metal through mass transport. The original oxygen in the slag was ignored.

2.2 VOF approach

We employed a VOF approach to track the movement of the slag–metal interfaces by solving a scalar field in the whole domain [12]:

$$\frac{\partial \alpha}{\partial t} + \nabla \cdot (\vec{v}\alpha) = 0, \tag{3}$$

where α represents the volume fraction and was updated at every time step. Meanwhile, the properties of the mixture phase, including electrical conductivity, density, and viscosity, were related to the volume fraction:

$$\bar{\phi} = \phi_m \alpha + \phi_s (1 - \alpha). \tag{4}$$

The continuum surface force model was used to describe the surface tension force between the metal and the slag.

2.3 Fluid flow and heat transfer

The continuity and time-averaged Navier–Stokes equations were used to describe the turbulent movements of the metal and the slag [17]:

$$\frac{\partial \bar{\rho}}{\partial t} + \nabla \cdot (\bar{\rho}\vec{v}) = 0 \tag{5}$$

$$\frac{\partial(\bar{\rho}\vec{v})}{\partial t} + \nabla \cdot (\bar{\rho}\vec{v} \otimes \vec{v}) = -\nabla p + \nabla \cdot [\mu(\nabla\vec{v} + \nabla\vec{v}^T)] + \vec{F}_{st} + \vec{F}_e + \vec{F}_s + \vec{F}_t \tag{6}$$

where \vec{F}_s and \vec{F}_t are the solutal and the thermal buoyancy forces, respectively, as determined by the Boussinesq approximation.

According to prior studies, the movement of slag and metal was, in most areas, under fully developed turbulence, and under weak turbulence in other areas [2, 10, 11]. For this paper, the standard $k-\epsilon$ turbulence model was developed for flows with a high Reynolds number, but did not meet the situation we encountered. However, with an appropriate treatment of the near-wall region, the RNG $k-\epsilon$ turbulence model is able to capture the behavior of flows with lower Reynolds numbers. Hence, in the present work turbulent viscosity is computed via the RNG $k-\epsilon$ turbulence

model. An enhanced wall function was also invoked herein to work with the RNG $k\text{-}\varepsilon$ turbulence model.

The energy conservation equation, shared between the two fluids, was [19]

$$\frac{\partial(\bar{\rho}E)}{\partial t} + \nabla \cdot (\vec{v}\bar{\rho}E) = \nabla \cdot (k_T \nabla T) + Q_J, \quad (7)$$

where E represents the internal energy of the mixture phase, which was solved based on the two phases' specific heat and temperature.

2.4 Mass transfer of oxygen

Oxygen convection and diffusion in the melt was described by [14, 20]

$$\frac{\partial(\bar{\rho}c)}{\partial t} + \nabla \cdot (\bar{\rho}\vec{v}c) = \nabla \cdot (\alpha D \nabla c) + S. \quad (8)$$

The equation was then established in the slag and in the metal, respectively. Both equations were solved simultaneously. The source term S indicated oxygen's mass transfer rate at the slag–metal interface. In order to satisfy mass conservation, the source terms in both equations were numerically equal but opposite in sign.

2.5 Kinetic module

An auxiliary metallurgical kinetic module was used to estimate the reaction rate [9]:

$$\text{Metal droplet–slag interface: } S = -\frac{nkF}{RT} |\vec{j}| \quad (9)$$

$$k = c_0 D^{0.5} \left(\frac{\varepsilon_\ell}{v_s} \right)^{0.25}. \quad (10)$$

Metal pool–slag interface:

$$S = +\frac{nkF}{RT} |\vec{j}| \quad (11)$$

$$k = c_0 D^{0.5} \left(\frac{\varepsilon_\ell}{v_m} \right)^{0.25} \quad (12)$$

Depending on the oxygen transfer direction, the source term had either a positive or a negative sign. We assumed that the source was positive when the oxygen moved from the metal to the slag. According to this migration pattern, the source was positive at the metal pool–slag interface and negative at the metal droplet–slag interface.

2.6 Electromagnetism

The current density distribution, required in Eqs. (9) and (11), was obtained by solving the electrical potential φ

from the current continuity equation and the Ohm's law [10, 21]:

$$\nabla \cdot (\bar{\sigma}\varphi) = 0 \quad (13)$$

$$\vec{J} = -\bar{\sigma} \nabla \varphi. \quad (14)$$

At the same time, the magnetic potential vector was introduced to solve the magnetic field:

$$\vec{B} = \nabla \times \vec{A}. \quad (15)$$

Therefore, Ampere's law $\nabla \times \vec{B} = \mu_0 \vec{J}$ could be rewritten as a Poisson equation:

$$-\nabla^2 \vec{A} = \mu_0 \vec{J}. \quad (16)$$

The magnetic field was obtained by combining Eqs. (15) and (16). Lorentz force and Joule heating were then expressed as:

$$\vec{F}_e = \vec{J} \times \vec{B} \quad (17)$$

$$Q_J = \frac{\vec{J} \cdot \vec{J}}{\bar{\sigma}}. \quad (18)$$

2.7 Boundary conditions

At the inlet, a varied mass flow rate was adopted, which was determined by the Joule heating [11]:

$$\dot{m} = \frac{\xi Q_J}{L}, \quad (19)$$

where ξ represents the power efficiency. Since power efficiency varies based on the operation conditions, it was difficult to estimate its exact value. A reasonable power efficiency was obtained from the reviewed literature, but was then adjusted according to the conditions of our experiment [22]. A no-slip condition was applied to both the wall and the bottom. On the top surface, zero shear stress was adopted.

A constant oxygen mass percent, equal to the oxygen content in the electrode used in our experiment, was supplied at the inlet. Using a zero-flux condition, we did not allow the oxygen to flow out through the wall or the bottom.

To simplify the consideration of metallic anode melting, the molten metal's temperature at the inlet was given by a parabolic profile. This profile was characterized by an approximate 30 K superheat and a peripheral boundary temperature close to the metal's liquid temperature [23]. We applied equivalent heat transfer coefficients to the top surface, wall, and the bottom.

We imposed a zero potential at the bottom while applying a potential gradient at the inlet [21]:

$$\frac{\partial \varphi}{\partial z} = I. \quad (20)$$

Table 1 Physical properties of metal and slag and the geometrical and operating conditions

Parameter	Value
Physical properties of metal	
Reference density, kg/m ³	7200
Viscosity, Pa·s	0.0061
Latent heat of fusion, kJ/kg	270
Thermal conductivity, W/m·K	30.52
Specific heat, J/kg·K	752
Electrical conductivity, Ω ⁻¹ ·m ⁻¹	7.14 × 10 ⁵
Magnetic permeability, H/m	1.257 × 10 ⁻⁶
Thermal coefficient of cubical expansion, K ⁻¹	1.1 × 10 ⁻⁴
Physical properties of slag	
Reference density, kg/m ³	2800
Viscosity, Pa·s	0.025
Thermal conductivity, W/m·K	10.46
Specific heat, J/kg·K	1255
Electrical conductivity, Ω ⁻¹ ·m ⁻¹	ln σ = -6769/T + 8.818
Magnetic permeability, H/m	1.257 × 10 ⁻⁶
Thermal coefficient of cubical expansion, K ⁻¹	5.4 × 10 ⁻⁴
Geometry	
Electrode diameter, m	0.055
Mold diameter, m	0.12
Slag pool height, m	0.06
Initial metal pool height, m	0.005

We assumed the top surface and wall to be electrically insulated [10]:

$$\frac{\partial \phi}{\partial |\vec{n}|} = 0. \tag{21}$$

The magnetic flux density was continuous at the top surface, inlet, and the bottom, and it was negligibly small at the wall [10]:

Top surface, inlet, and bottom:

$$A_x = A_y = \frac{\partial A_z}{\partial z} = 0 \tag{22}$$

Wall:

$$A_x = A_y = A_z = 0, \tag{23}$$

where A_x , A_y , and A_z are the magnetic potential vectors along the x -, y -, and z -axes, respectively. Table 1 lists the detailed physical properties and geometrical and operating conditions.

3 Numerical treatment

We used the commercial software ANSYS-FLUENT 12.1 to run the simulation. Using an iterative procedure, the

governing equations for electromagnetism, two-phase flow, heat transfer, and solute transport were integrated over each control volume and solved simultaneously. Through user-defined functions, we implemented the introduction of the magnetic potential vector, as well as the development of the kinetic module. The widely used SIMPLE algorithm was employed for calculating the Navier–Stokes equations. We discretized all the equations by the second-order upwind scheme to ensure higher accuracy. Before moving on to the next step, the iterative procedure continued until all normalized unscaled residuals were less than 10⁻⁶. Due to the metal droplet’s falling, the metal pool’s height was prone to increasing with time. To consider the computational domain growth, a dynamic mesh was therefore adopted. The control volumes’ top row spawned a new row once it was 1.25 times the height of the other rows. We thoroughly tested the mesh independence. Three families of structured meshes were generated, with the respective sizes of 2, 4, and 7 mm. After a typical simulation, the velocity and temperature of some points in the domain were carefully compared. The deviation of simulated results between the first and second mesh was about 4 pct, while it was approximately 10 pct between the second and third mesh. Furthermore, the value of y^+ within the grids adjacent to the wall was equal to ~1. Therefore, considering the high expense of computation, we retained the second mesh to use throughout the rest of this work. Figure 2 shows the mesh at its initial state. Due to the complexity of the coupling calculation, we kept a small time step to ensure that the above converge criteria were fulfilled. Using 8 cores of 3.40 GHz, the calculations for a typical case took approximately 610 CPU hours.

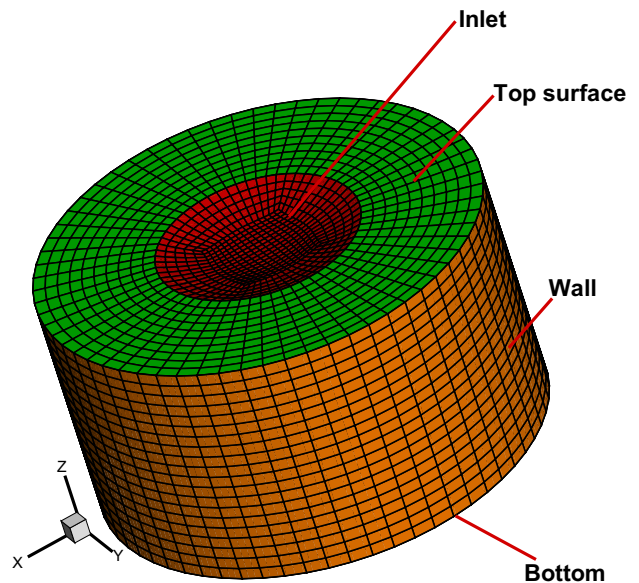


Fig. 2 Mesh and boundaries

4 Experiment

We carried out an experiment using a mold with an open-air atmosphere as displayed in Fig. 3. The mold was produced by the copper, and its inner diameter, height, and lateral wall thickness were 120, 600, and 65 mm, respectively. In the experiment, the mold and the baseplate were cooled by the water. The electrode was the AISI 201 stainless steel bar with a 55 mm diameter. The slag was composed of 70 mass % calcium fluoride and 30 mass % alumina, and the thickness of the slag layer remained constant at 60 mm. The current used in the experiment was 1800 A, and the direct current flowed from the electrode to the baseplate. During the experiment, we used a syringe and a quartz glass

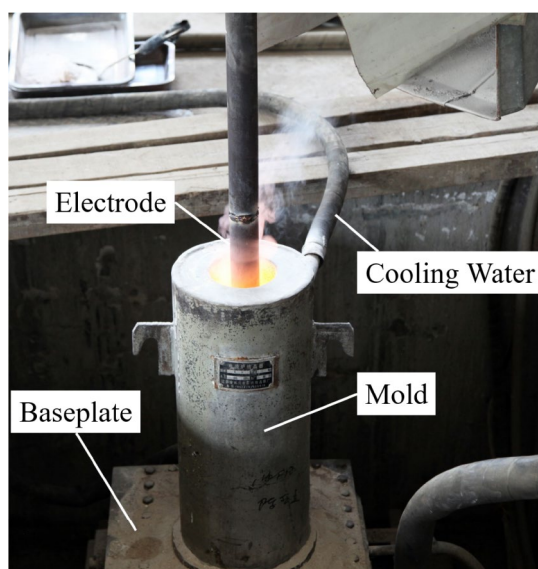
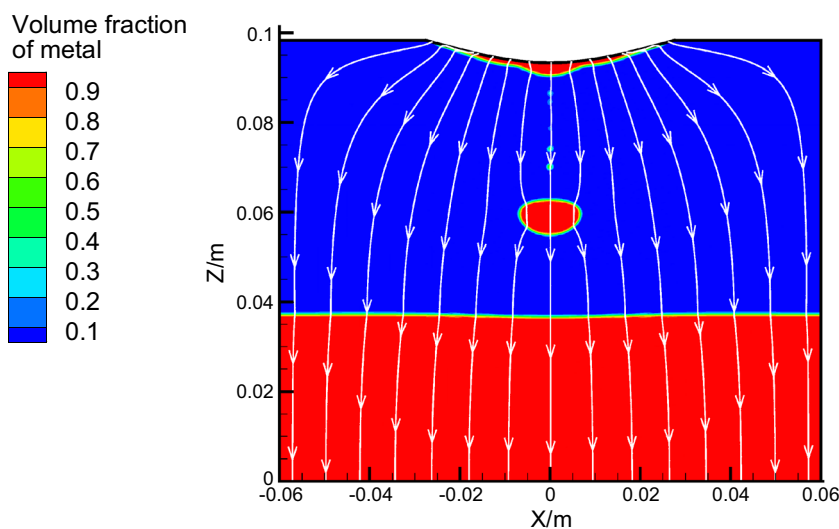


Fig. 3 Experimental device

Fig. 4 Distributions of the electric streamlines and the phase distribution at 151.25 s with a current of 1800 A



tube to obtain samples from the slag and the metal, respectively. After cooling, the oxygen content in the samples was measured by an oxygen and nitrogen analyzer (LECO, St. Joseph, MO, USA).

5 Results and discussion

At the beginning of the simulation, a 60-mm slag and 5-mm metal layers without oxygen were observed. The metal containing 0.024% oxygen entered the domain from the inlet once the computation was started. The above initial oxygen content was supposed to be equal to the oxygen mass percent in the electrode used in our experiment. The solidification, ignored in our simulation, would affect the oxygen content in the metal. In order to eliminate this influence, the total time of the simulated process was controlled to be within 240 s, and during this time, the solidification did not yet occur in the experiment. Besides, the metal droplet periodically dropped down during the process, and the growth and detachment of the droplet could be observed in each cycle. The change of the oxygen content however was less obvious at the early stage, and thus we chose to display the results at the later period.

Figure 4 illustrates the electric current streamlines and phase distribution with a current of 1800 A at 151.25 s. Once the current enters the domain, it spreads around and then flows downward. The metal significantly influences the current's movement due to its higher electrical conductivity. It can be seen that the current streamlines are distorted when traveling through the metal droplet. The current within the droplet flows mainly parallel to the axis, somewhat converging in the droplet's upper part and diverging in the lower part.

Figure 5 shows the flow pattern and temperature distribution. We can observe a clockwise circulation in the slag layer in the wall's vicinity. The heat in this area is likely reduced by the cooling water, resulting in the sinking of colder slag. Simultaneously, the inward Lorentz force along with the falling droplet creates a counterclockwise cell at the slag's center.

The slag around the inlet generates more Joule heating due to a higher current density and larger electrical resistance. The slag located at the top layer is therefore much hotter, with a highest temperature of approximately 2150 K. The hotter slag, in turn, would heat the colder metal droplet during the falling process. Thus, the slag's temperature in the middle is lower.

The temperature of the metal is lower than that of the slag due to a lower Joule heat. Cooling water at the wall and the bottom extracts a large amount of heat. Metal at the outer layer is therefore colder than metal at the inner layer. The temperature difference drives the metal along the slag–metal interface toward the outer edge and, from there, down along the wall. At the base of the pool, the metal flows back to the center and then turns up toward the slag–metal interface.

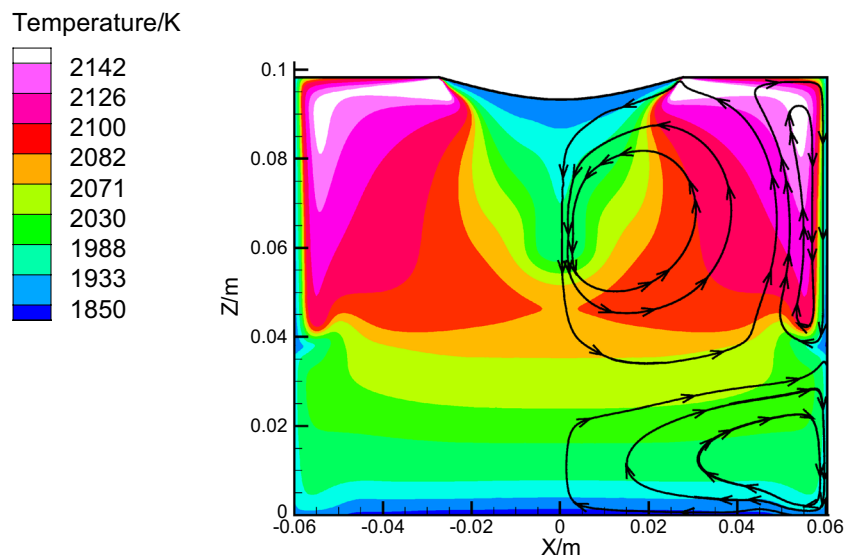
Figures 6 and 7 indicate the distribution of the oxygen's mass percent in the metal and the slag at different time instants. Oxygen transport behavior can be found at the two slag–metal interfaces. The upper one is the metal droplet–slag interface and the lower one is the metal pool–slag interface. As stated above, electrons' movement directions at both interfaces are opposite. Oxygen ions in the slag typically become atoms and go into the metal droplet when the electrons travel through the metal droplet–slag interface. Hence, the oxygen content in the metal droplet increases. As shown in Fig. 6a, the metal closest to the droplet tip has

a higher oxygen concentration. When the droplet grows, the oxygen in the slag is continuously transferred into the metal. In Fig. 6b, the oxygen content in the lower part of the droplet is approximately 1.2 times higher than its original content. Additionally, the oxygen transfer is supposed to be accelerated during the formation of the droplet. This is because the specific surface area tends to increase, while the current density around the droplet becomes higher. When the droplet hits the metal pool–slag interface, the oxygen spreads out in the metal pool. Its distribution is then controlled by the flow pattern shown in Fig. 6d. At the metal pool–slag interface, the oxygen atoms in the metal pool would capture two electrons and enter into the slag in ion status, resulting in an oxygen content drop. The oxygen concentration in the metal pool is therefore determined by the oxygen concentration in the droplet as well as the transport rate at the metal pool–slag interface.

In the slag layer, the minimum oxygen content is found in the slag around the droplet, possibly due to the transport behavior that is indicated in Fig. 7. The content gradually rises when the slag layer's outer side expands. Moreover, the slag close to the metal pool–slag interface contains more oxygen, which comes from the metal pool.

According to the above findings, we may conclude that the final oxygen content in the metal and the slag is determined by the two transfer rates. Fig. 8a, b illustrates the transfer rates of the two interfaces at 151.16 s. At the metal droplet–slag interface, a negative transfer rate is found, while a positive rate is observed at the metal pool–slag interface. Moreover, the rate at the upper interface is approximately one order of magnitude higher than that at the lower interface. This can be attributed to the significant influence on the lower interface's rate by the current density, as shown in Fig. 9. It is obvious that

Fig. 5 Distributions of the flow streamlines and the temperature at 151.25 s with a current of 1800 A



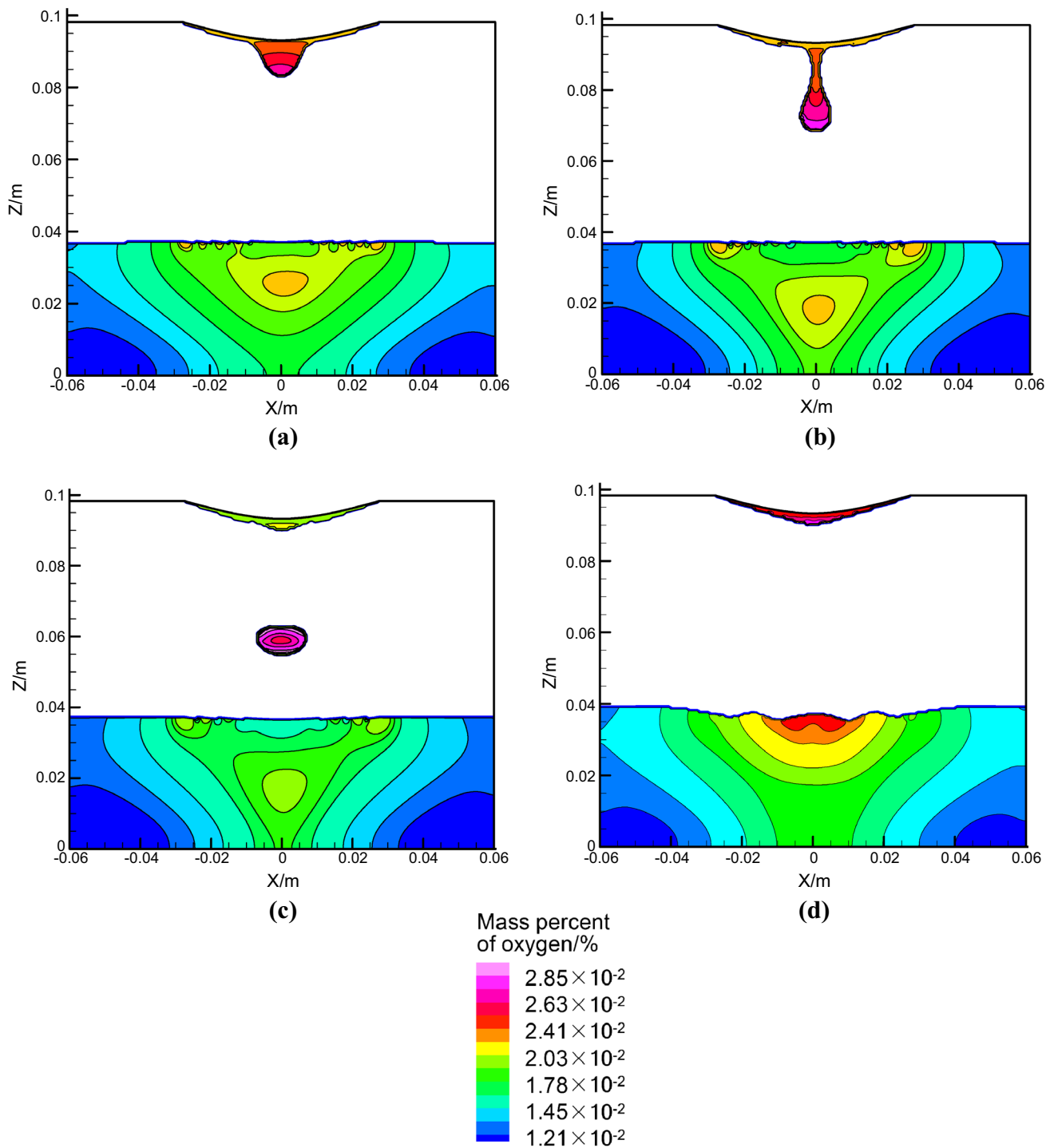


Fig. 6 Evolution of oxygen concentration in the metal with time when the current is 1800 A: **a** 150.53 s, **b** 151.16 s, **c** 151.25 s, and **d** 151.49 s

the current density at the metal droplet–slag interface is about an order of magnitude larger than that at the metal pool–slag interface. The negative transfer rate is supposedly larger than the positive one; as a result, the amount of oxygen carried by the droplet is larger than that lost through the metal pool–slag interface.

Figure 10 demonstrates the evolution of oxygen concentration in time at point 1. Clearly, the final oxygen concentration in the metal pool increases over time. We also measured the oxygen content of point 1 in the experiment. The variation tendency of the two results is the same, but the measured values are slightly larger. Actually, some active

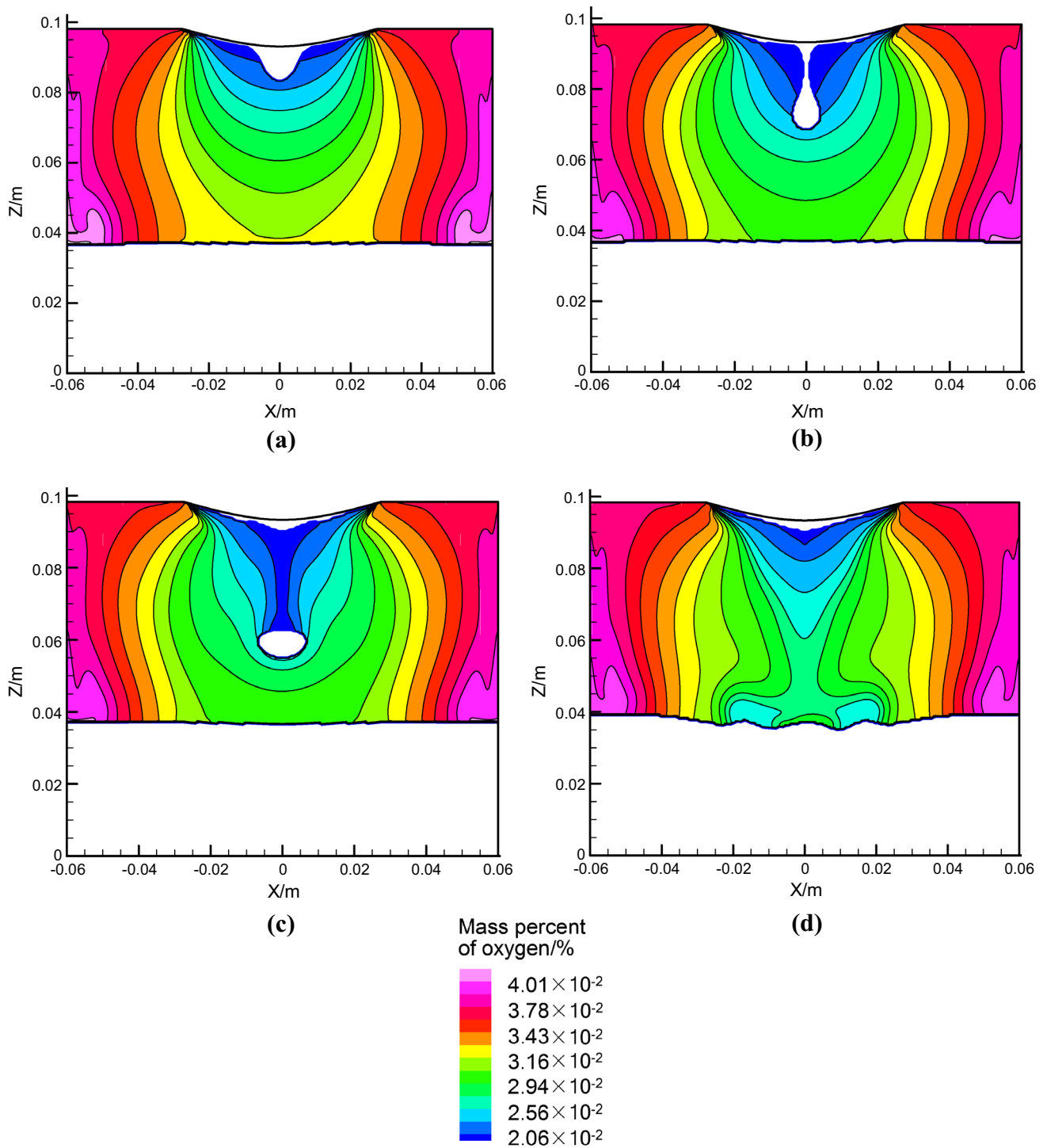


Fig. 7 Evolution of oxygen concentration in the slag with time when the current is 1800 A: **a** 150.53 s, **b** 151.16 s, **c** 151.25 s, and **d** 151.49 s

elements in the metal droplet such as aluminum, silicon, and manganese would react with the oxygen in the slag during its falling due to the drop of Gibbs free energy. Hence, the oxygen would be brought into the metal pool, resulting in an increase of the content. These chemical reactions however were ignored in the simulation.

Figure 11 shows the oxygen concentration variation at time points 2 and 3. As expected, the content of these two points has a decreasing trend. A reasonable agreement between the experimental results and the simulated results is obtained. In practical, a few amount of aluminum oxide in the slag would be decomposed into dissolved aluminum and oxygen under

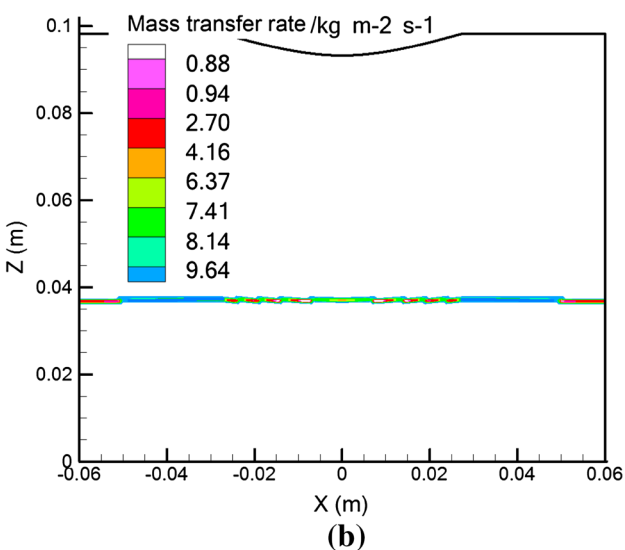
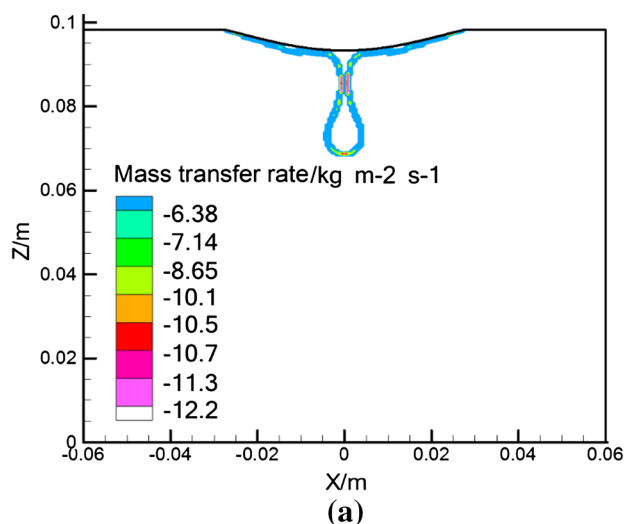
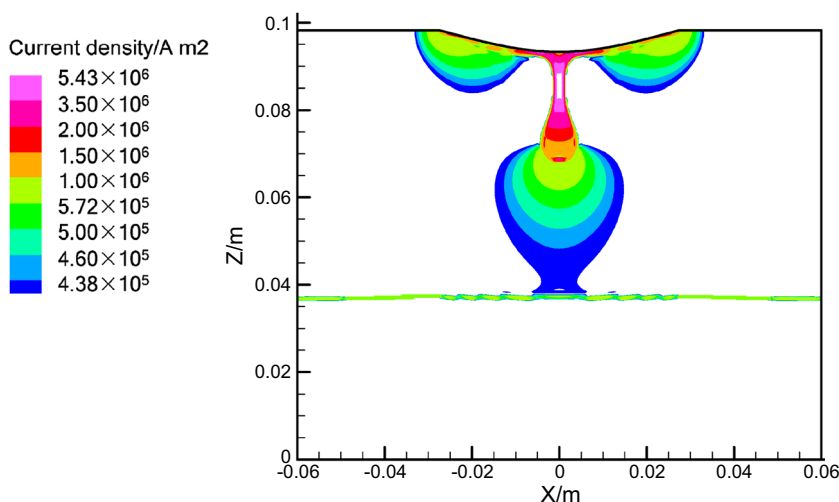


Fig. 8 Mass transfer rate between the slag and the metal with 1800 A current at 151.16 s: **a** metal droplet–slag interface and **b** metal pool–slag interface

Fig. 9 Current density distribution with a current of 1800 A at 151.16 s



the effect of the high temperature. The dissolved aluminum is then easy to react with the oxygen in the air. With the influences of these two aspects, the measured data are greater than the simulated data we were able to obtain.

The obtained results indicate that the oxygen in the metal could be barely removed by the current in the electro-slag refining process. Due to the opposite direction of the electrochemical reaction, the oxygen removed from the metal pool would reenter the metal droplet. Therefore, we propose to add one more positive electrode in the unit, which is more likely to react with the oxygen. As a result, oxygen in the slag would shift into the more active electrode rather than the metal droplet, and thus oxygen can be effectively taken away. Detailed research would be implemented in our next work.

6 Conclusions

This study established a transient 3D coupled mathematical model to study oxygen transport behavior in the electro-slag refining process. The finite volume method was used to simultaneously compute the mass, momentum, energy, and species conservation equations. The Joule heating and Lorentz force were fully coupled through solving Maxwell’s equations with the assistance of the magnetic potential vector. The movement of the metal–slag interface was described using the VOF approach. Moreover, an auxiliary metallurgical kinetic module was introduced to determine the electrochemical reaction rate. In the course of this study, an experiment was conducted to verify the proposed model. Given the obtained results, the predicted oxygen contents match with the measured data within an acceptable range of accuracy. The oxygen ions in the slag are transferred into the droplet as atoms through the metal droplet–slag interface. Meanwhile, the oxygen atoms in the

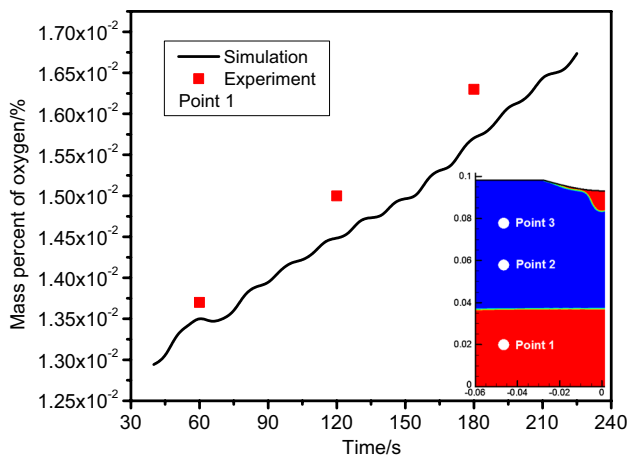


Fig. 10 Evolution of oxygen concentration with time at point 1 when the current is 1800 A

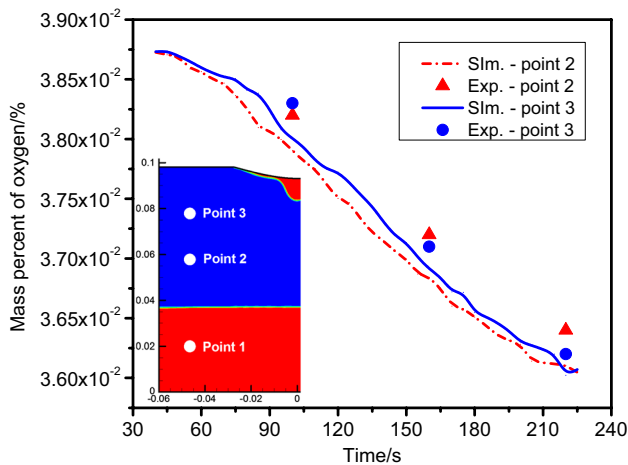


Fig. 11 Evolution of oxygen concentration with time at points 2 and 3 when the current is 1800 A

metal pool capture two electrons and become oxygen ions, which then travel through the metal pool–slag interface. The negative transfer rate at the metal droplet–slag interface is approximately one order of magnitude larger than the positive one at the metal pool–slag interface. Therefore, the oxygen content in the metal pool exhibits an increasing trend, with the content in the slag exhibiting a decreasing trend, particularly with prolonged time. In order to effectively remove the oxygen in the metal, one more positive electrode, which is more likely to react with the oxygen, is proposed to be added in the unit.

Acknowledgements The authors’ gratitude goes to the National Natural Science Foundation of China (Grant No. 51210007) and the Key Program of Joint Funds of the National Natural Science Foundation of China and the Government of Liaoning Province (Grant No. U1508214).

References

- Ludwig A, Kharicha A, Wu M (2014) Modeling of multiscale and multiphase phenomena in materials processing. *Metall Mater Trans B* 45:36–43
- Weber V, Jardy A, Dussoubs B, Ablitzer D, Rybéron S, Schmitt V, Hans S, Poisson H (2009) A comprehensive model of the electroslag remelting process: description and validation. *Metall Mater Trans B* 40:271–280
- Shi C B, Chen X C, Guo H J, Zhu Z J, Ren H (2012) Assessment of oxygen control and its effect on inclusion characteristics during electroslag remelting of die steel. *Steel Res Int.* 83:472–486
- Chang LZ, Shi XF, Yang HS, Li ZB (2009) Effect of low-frequency AC power supply during electroslag remelting on qualities of alloy steel. *J Iron Steel Res Int* 16:7–11
- Goldstein D A, Fruehan R J (1999) Mathematical model for nitrogen control in oxygen steelmaking. *Metall Mater Trans B* 30:945–956
- Wei J H, Mitchell A (1984) Changes in composition during AC ESR—II. laboratory results and analysis. *Acta Metall Sin* 20:280–287
- Kato M, Hasegawa K, Nomura S, Inouye M (1983) Transfer of oxygen and sulfur during direct current electroslag remelting. *Trans ISIJ* 23:618–627
- Kawakami M, Takenaka T, Ishikawa M (2002) Electrode reactions in dc electroslag remelting of steel rod. *Ironmak Steelmak* 29:287–292
- Zhang G H, Chou K C, Li F S (2014) Deoxidation of liquid steel with molten slag by using electrochemical method. *ISIJ Int* 54:2767–2771
- Kharicha A, Wu M, Ludwig A, Karimi-Sibaki E (2016) Simulation of the electric signal during the formation and departure of droplets in the electroslag remelting process. *Metall Mater Trans B* 47:1427–1434
- Wang Q, Zhao RJ, Fafard M, Li BK (2015) Three-dimensional magnetohydrodynamic two-phase flow and heat transfer analysis in electroslag remelting process. *Appl Therm Eng* 80:178–186
- Yanke J, Fezi K, Trice R W, Krane M J M (2015) Simulation of slag-skin formation in electroslag remelting using a volume-of-fluid method. *Numer Heat Tr A-Appl* 67:268–292
- Dong Y W, Jiang Z H, Cao H B, Wang X, Cao Y L, Hou D (2016) A novel single power two circuits electroslag remelting with current carrying mould. *ISIJ Int* 56:1386–1393
- Jonsson L, Sichen D, Jönsson P (1998) A new approach to model sulfur refining in a gas-stirred ladle—a coupled CFD and thermodynamic model. *ISIJ Int* 38:260–267
- Danilov V A (2016) Numerical investigation of combined chemical and electrochemical processes in Fe_2O_3 suspension electrolysis. *J Appl Electrochem* 46:85–101
- Sen D, Isaac KM, Leventis N, Fritsch I (2011) Investigation of transient redox electrochemical MHD using numerical simulations. *Int J Heat Mass Transfer* 54:5368–5378
- Hernandez-Morales B, Mitchell A (1999) Review of mathematical models of fluid flow, heat transfer, and mass transfer in electroslag remelting process. *Ironmak Steelmak* 26:423–438
- Wang Q, He Z, Li GQ, Li BK, Zhu CY, Chen PJ (2017) Numerical investigation of desulfurization behavior in electroslag remelting process. *Int J Heat Mass Transfer* 104:943–951
- Byon C (2014) Numerical study on the phase change heat transfer of LNG in glass wool based on the VOF method. *Int J Heat Mass Transfer* 88:20–27
- Lou W T, Zhu M Y (2014) Numerical simulation of desulfurization behavior in gas-stirred systems based on computation fluid dynamics-simultaneous reaction model coupled model. *Metall Mater Trans B* 45:1706–1722

21. Dilawari AH, Szekely J, Eagar TW (1978) Electromagnetically and thermally driven flow phenomena in electroslag welding. *Metall Trans B* 9:371–381
22. Wang Q, He Z, Li B K, Tsukihashi F (2014) A general coupled mathematical model of electromagnetic phenomena, two-phase flow, and heat transfer in electroslag remelting process including conducting in the mold. *Metall Mater Trans B* 45:2425–2441
23. Mitchell A (2005) Solidification in remelting processes. *Mater Sci Eng A* 413–414:10–18